



HAL
open science

Close evaluation of layer potentials in three dimensions

Shilpa Khatri, Arnold D Kim, Ricardo Cortez, Camille Carvalho

► **To cite this version:**

Shilpa Khatri, Arnold D Kim, Ricardo Cortez, Camille Carvalho. Close evaluation of layer potentials in three dimensions. *Journal of Computational Physics*, 2020, 423, pp.109798. hal-01832316

HAL Id: hal-01832316

<https://hal.science/hal-01832316>

Submitted on 7 Jul 2018

HAL is a multi-disciplinary open access archive for the deposit and dissemination of scientific research documents, whether they are published or not. The documents may come from teaching and research institutions in France or abroad, or from public or private research centers.

L'archive ouverte pluridisciplinaire **HAL**, est destinée au dépôt et à la diffusion de documents scientifiques de niveau recherche, publiés ou non, émanant des établissements d'enseignement et de recherche français ou étrangers, des laboratoires publics ou privés.

Close evaluation of layer potentials in three dimensions

Camille Carvalho* Shilpa Khatri * Arnold D. Kim *

July 6, 2018

Abstract

We present a simple and effective method for computing double- and single-layer potentials for Laplace's equation in three dimensions close to the boundary. The close evaluation of these layer potentials is challenging because they are nearly singular integrals. The method is comprised of three steps: (i) rotate the spherical coordinate system so that the peak of the kernel in the nearly-singular integral is aligned with its north pole; (ii) integrate first with respect to azimuth using the Periodic Trapezoid Rule, which is a natural averaging operation yielding a relatively smooth function of the polar angle; and (iii) integrate with respect to the polar angle (rather than the cosine of the polar angle) using an open, Gauss-Legendre quadrature rule mapped to $[0, \pi]$. We find that the asymptotic behavior of the error for this method in the limit of small evaluation distance from the boundary is quadratic for the modified double-layer potential after applying a subtraction method to it, and linear for the single-layer potential. Additionally, we use this method for computing the matrix entries of the Galerkin method to solve the underlying boundary integral equations. We illustrate the accuracy and utility of this method through several numerical examples.

Keywords: Nearly singular integrals, close evaluation problem, potential theory, boundary integral equations, numerical quadrature.

1 Introduction

The close evaluation problem arises in boundary integral methods for numerically solving boundary value problems for linear, elliptic partial differential equations. In boundary integral equation methods, the solution of the boundary value problem is given in terms of double- and single-layer potentials, which are integrals of a kernel multiplied by a density over the boundary of the domain. The kernel for the single-layer potential is the fundamental solution of the elliptic, partial differential equation and the kernel for the double-layer potential is the normal derivative of that fundamental solution. As a result, each of these kernels has an isolated singularity at a known point on the boundary. When evaluating double- and single-layer potentials at points close to the boundary, the associated kernel is regular, but is sharply peaked because the evaluation point is close to its singular point on the boundary. For this reason, we say that double- and single-layer potentials evaluated close to the boundary are nearly singular integrals.

Nearly singular integrals are more challenging to compute numerically than weakly singular ones. When computing weakly singular integrals, one must explicitly address the singularity in the kernel. For example, weakly singular integrals can be computed accurately using high-order product Nyström methods [7, 14]. These product Nyström methods are often used to solve the boundary integral equations for the density. However, for a nearly singular integral, there is no singularity to address. Nonetheless, without effectively addressing the peak in a nearly singular integral, one must increase

*Applied Mathematics Unit, School of Natural Sciences, University of California, Merced, 5200 North Lake Road, Merced, CA 95343

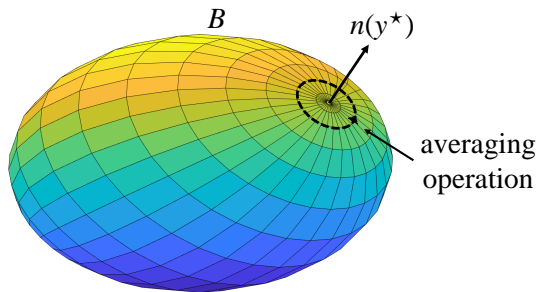


Figure 1: The point y^* on the boundary surface denoted by B , indicated by the outward, unit normal, $n(y^*)$. Even though the fundamental solution for Laplace’s equation and its normal derivative are singular at y^* , integration over B includes a natural averaging operation about y^* indicated by the dashed closed curve. This averaging operation is important for computing the close evaluation of double- and single-layer potentials in three dimensions.

the order of the quadrature rule to obtain accuracy commensurate with evaluation points that are far from the boundary.

The close evaluation problem has been studied extensively. Schwab and Wendland [20] have developed a boundary extraction method based on a Taylor series expansion of the layer potentials. Beale and Lai [9] have developed a method that first regularizes the nearly singular kernel and then adds corrections for both the discretization and the regularization. The result of this approach is a uniform error in space. Helsing and Ojala [17] developed a method that combines a globally compensated quadrature rule and interpolation to achieve very accurate results over all regions of the domain. Barnett [8] has used surrogate local expansions with centers placed near, but not on, the boundary. This work led to the work by Klöckner *et al.* [18] that introduces Quadrature By Expansion (QBX). QBX uses expansions about accurate evaluation points far away from the boundary to compute accurate evaluations close to it. The convergence of QBX has been studied in [15]. Moreover, fast implementations of QBX have since been developed [1, 19, 21], and rigorous error estimates have been derived for the method [2]. Recently, the authors developed a method that involved matched asymptotic expansions for the kernel [12]. In that method, the asymptotic expansion that captures the peaked behavior of the kernel can be integrated exactly and the relatively smooth remainder is integrated numerically, resulting in a highly accurate method.

Most of these aforementioned studies are for two-dimensional problems. There are fewer results for three-dimensional problems. Beale *et al.* [10] have extended the regularization method to three-dimensional problems. Additionally, QBX has been used for three-dimensional problems [1, 21]. In principle, the matched asymptotic expansion method by the authors can be extended to three dimensional problems. However, we do not pursue that approach because the method we present here is more direct and simpler to implement.

We study the close evaluation of double- and single-layer potentials in the context of the interior Dirichlet and exterior Neumann problems for Laplace’s equation in three dimensions, respectively. Compared to the close evaluation of layer potentials in two dimensions, we find that layer potentials in three dimensions are actually better behaved because the double integral over the boundary naturally includes an averaging operation about y^* , the point on the boundary at which the kernels have a singularity (see Fig. 1). This averaging operation is a crucial aspect of the layer potential’s representation of a harmonic function that smoothly approaches its boundary data. To find this inherent averaging operation, we perform a local analysis of the contribution of the layer potentials in the vicinity of y^* . This local analysis provides valuable insight into the close evaluation problem and suggests a natural method for numerically computing nearly singular layer potentials in three dimensions. We also find that this method can be used to compute weakly singular integrals, in particular for numerically solving the boundary integral equation for densities.

The remainder of this paper is as follows. We precisely define the close evaluation problem for the double- and single-layer potentials in Section 2. In Section 3, we compute the asymptotic behavior of the contributions to these layer potentials made by a small region containing the point where the kernels are peaked. By doing so, we find a natural numerical method to evaluate these nearly singular integrals. This numerical method is detailed in Section 4. We discuss in Section 5 how this method can also be used to compute matrix entries in the Galerkin method to solve the boundary integral equations for the densities. We give several examples demonstrating the accuracy of this numerical method in Section 6. Section 7 gives our conclusions. A gives details of how we rotate spherical integrals in the results presented in this paper, and B gives a useful derivation of the spherical Laplacian.

2 Close evaluation of double- and single-layer potentials

Consider a simply connected, open set denoted by $D \subset \mathbb{R}^3$ with boundary, B , and let $\bar{D} = D \cup B$. For some given smooth data f , we write the function $u \in C^2(D) \cap C^1(\bar{D})$ satisfying the interior Dirichlet problem,

$$\begin{aligned} \Delta u &= 0 && \text{in } D, \\ u &= f && \text{on } B, \end{aligned} \tag{2.1}$$

as the double-layer potential,

$$u(x) = \frac{1}{4\pi} \int_B \frac{n(y) \cdot (x - y)}{|x - y|^3} \mu(y) d\sigma_y, \quad x \in D, \tag{2.2}$$

with $n(y)$ denoting the unit, outward normal at $y \in B$, and $d\sigma_y$ denoting the surface element. Here, μ is the density for the double-layer potential satisfying

$$-\frac{1}{2}\mu(y^*) + \frac{1}{4\pi} \int_B \frac{n(y) \cdot (y^* - y)}{|y^* - y|^3} \mu(y) d\sigma_y = f(y^*), \quad y^* \in B. \tag{2.3}$$

Let $E = \mathbb{R}^3 \setminus \bar{D}$, and $\bar{E} = E \cup B$. Let n still denote the unit normal pointing outward from D . For some given smooth data g , we write the function $v \in C^2(E) \cap C^1(\bar{E})$ satisfying the exterior Neumann problem,

$$\begin{aligned} \Delta v &= 0 && \text{in } E, \\ -\partial_n v &= g && \text{on } B, \end{aligned} \tag{2.4}$$

as the single-layer potential,

$$v(x) = \frac{1}{4\pi} \int_B \frac{\rho(y)}{|x - y|} d\sigma_y, \quad x \in E. \tag{2.5}$$

Here, $\rho(y)$ is the density for the single-layer potential satisfying

$$\frac{1}{2}\rho(y^*) - \frac{1}{4\pi} \int_B \frac{n(y^*) \cdot (y^* - y)}{|y^* - y|^3} \rho(y) d\sigma_y = g(y^*), \quad y^* \in B, \tag{2.6}$$

Boundary integral equation methods involve solving (2.3) and (2.6) for μ and ρ , respectively. These results are then used to compute u using (2.2) for any desired point in D and v using (2.5) for any desired point in E . Boundary integral equations (2.3) and (2.6) can be solved to very high accuracy using Nyström methods [7, 14]. Thus, the focus turns to accurately computing the double- and single-layer potentials, (2.2) and (2.5), respectively. The high accuracy of Nyström methods transfers over to the evaluation of these layer potentials except for close evaluation points.

To define a close evaluation point precisely, let $0 < \varepsilon \ll 1$ denote a small, dimensionless parameter, and consider

$$x = y^* \mp \varepsilon \ell n^*, \tag{2.7}$$

for $x \in D$ and $x \in E$, respectively, with $y^* \in B$ denoting a point on the boundary, $n^* = n(y^*)$ denoting the unit, outward normal from D at y^* , and ℓ denoting a characteristic length of B , *e.g.* its radius of curvature at y^* . Before substituting (2.7) into (2.2), we first make use of Gauss' law [16],

$$\frac{1}{4\pi} \int_{\partial D} \frac{n(y) \cdot (x - y)}{|x - y|^3} d\sigma_y = \begin{cases} -1 & x \in D, \\ -\frac{1}{2} & x \in B, \\ 0 & x \in E, \end{cases} \quad (2.8)$$

to write the double-layer potential evaluated at the close evaluation point given in (2.7) as

$$u(y^* - \varepsilon \ell n^*) = -\mu(y^*) + \frac{1}{4\pi} \int_B \frac{n(y) \cdot (y^* - y - \varepsilon \ell n^*)}{|y^* - y - \varepsilon \ell n^*|^3} [\mu(y) - \mu(y^*)] d\sigma_y. \quad (2.9)$$

We call (2.9) the modified double-layer potential resulting from applying a subtraction method [14]. For the close evaluation of the single-layer potential, we substitute (2.7) into (2.5) and obtain

$$v(y^* + \varepsilon \ell n^*) = \frac{1}{4\pi} \int_B \frac{\rho(y)}{|y^* - y + \varepsilon \ell n^*|} d\sigma_y. \quad (2.10)$$

Our objective here is the accurate and efficient numerical evaluation of (2.9) and (2.10). The challenge in this problem is that in the asymptotic limit as $\varepsilon \rightarrow 0$, those integrals are nearly singular. Setting $\varepsilon = 0$ yields weakly singular integrals which can be numerically evaluated accurately. In fact, this is what is done in the Nyström method to solve boundary integral equations (2.3) and (2.6). However, when ε is small, but finite, the functions to be integrated are not singular, but they are sharply peaked about $y = y^*$ which makes computing (2.9) and (2.10) challenging.

3 Motivation: local analysis of the double- and single-layer potentials at a close evaluation point

The nearly singular behavior of (2.9) and (2.10) about $y = y^*$ is the major cause for error in their evaluation. For this reason, we analyze the contribution made by a small region about $y = y^*$. By doing so, we motivate the method that we use to evaluate (2.9) and (2.10). In general, it is more challenging to evaluate the double-layer potential than the single-layer potential because the kernel in (2.9) is more peaked than that in (2.10). However, we show below that the modified double-layer potential given in (2.9) will have a more accurate evaluation than (2.10) due to the subtraction method that has been used.

For simplicity, suppose that B is an analytic, closed, and oriented surface. This assumption can be relaxed to just local smoothness about y^* with appropriate technical modifications. We introduce the parameters $s \in [0, \pi]$ and $t \in [-\pi, \pi]$ for a rotated spherical coordinate system that parametrizes B such that $y^*/|y^*|$ corresponds to the north pole, *i.e.* $y = y(s, t)$ and $y^* = y(0, \cdot)$. Details about this rotated coordinate system can be found in A. In terms of this parameterization, (2.9) is given by

$$u(y^* - \varepsilon \ell n^*) = -\tilde{\mu}(0, \cdot) + \frac{1}{4\pi} \int_{-\pi}^{\pi} \int_0^{\pi} K(s, t; \varepsilon) [\tilde{\mu}(s, t) - \tilde{\mu}(0, \cdot)] \sin(s) ds dt, \quad (3.1)$$

with $\tilde{\mu}(s, t) = \mu(y(s, t))$, $\tilde{\mu}(0, \cdot) = \mu(y(0, \cdot))$, and

$$K(s, t; \varepsilon) = \frac{\tilde{n}(s, t) \cdot (y_d(s, t) - \varepsilon \ell n^*)}{|y_d(s, t) - \varepsilon \ell n^*|^3} J(s, t), \quad (3.2)$$

with $\tilde{n}(s, t) = n(y(s, t))$, $y_d(s, t) = y(0, \cdot) - y(s, t)$, and $J(s, t) = |y_s(s, t) \times y_t(s, t)| / \sin(s)$. In the limit as $\varepsilon \rightarrow 0$, this kernel becomes sharply peaked for $y_d = O(\varepsilon)$ leading to $K = O(\varepsilon^{-2})$. This behavior characterizes this nearly singular integral.

We consider the contribution to u made by a small portion of B about $y = y^*$, which we denote by U . To do so, we introduce the parameter $\delta > 0$ and define

$$U(y^*; \varepsilon, \delta) = \frac{1}{4\pi} \int_{-\pi}^{\pi} \int_0^{\delta} K(s, t; \varepsilon) [\tilde{\mu}(s, t) - \tilde{\mu}(0, \cdot)] \sin(s) \, ds dt. \quad (3.3)$$

Next, we substitute $s = \varepsilon S$ in (3.3), and find

$$U(y^*; \varepsilon, \delta) = \frac{1}{4\pi} \int_{-\pi}^{\pi} \int_0^{\delta/\varepsilon} K(\varepsilon S, t; \varepsilon) [\tilde{\mu}(\varepsilon S, t) - \tilde{\mu}(0, \cdot)] \sin(\varepsilon S) \varepsilon \, dS dt. \quad (3.4)$$

Recognizing that $\tilde{n}(\varepsilon S, t) = n^* + O(\varepsilon)$, and $y_d(\varepsilon S, t) = -\varepsilon S y_s(0, \cdot) + O(\varepsilon^2)$ with $y_s(0, \cdot) \neq 0$ lying on the plane tangent to B at y^* , we find by expanding $K(\varepsilon S, t; \varepsilon)$ about $\varepsilon = 0$ that

$$K(\varepsilon S, t; \varepsilon) = -\frac{\ell J(0, \cdot)}{\varepsilon^2} \frac{1}{(S^2 |y_s(0, \cdot)|^2 + \ell^2)^{3/2}} + O(\varepsilon^{-1}). \quad (3.5)$$

Substituting this leading-order behavior into (3.4) along with $\sin(\varepsilon S) = \varepsilon S + O(\varepsilon^3)$, we obtain

$$U(y^*; \varepsilon, \delta) = -\frac{\ell J(0, \cdot)}{4\pi} \int_{-\pi}^{\pi} \int_0^{\delta/\varepsilon} \left[\frac{S}{(S^2 |y_s(0, \cdot)|^2 + \ell^2)^{3/2}} + O(\varepsilon) \right] [\tilde{\mu}(\varepsilon S, t) - \tilde{\mu}(0, \cdot)] \, dS dt. \quad (3.6)$$

Since the leading-order asymptotic behavior given in (3.5) is independent of t , we use the 2π -periodicity of $\tilde{\mu}$ with respect to t to write

$$U(y^*; \varepsilon, \delta) = -\frac{\ell J(0, \cdot)}{4\pi} \int_0^{\delta/\varepsilon} \left\{ \left[\frac{S}{(S^2 |y_s(0, \cdot)|^2 + \ell^2)^{3/2}} + O(\varepsilon) \right] \left[\int_0^{\pi} \tilde{\mu}(\varepsilon S, t) + \tilde{\mu}(\varepsilon S, t - \pi) - 2\tilde{\mu}(0, \cdot) dt \right] \right\} dS. \quad (3.7)$$

Next, we use the regularity of $\tilde{\mu}$ over the north pole to substitute $\tilde{\mu}(\varepsilon S, t - \pi) = \tilde{\mu}(-\varepsilon S, t)$, and find that

$$\begin{aligned} U(y^*; \varepsilon, \delta) &= -\frac{\ell J(0, \cdot)}{4\pi} \int_0^{\delta/\varepsilon} \left\{ \left[\frac{S}{(S^2 |y_s(0, \cdot)|^2 + \ell^2)^{3/2}} + O(\varepsilon) \right] \left[\int_0^{\pi} \tilde{\mu}(\varepsilon S, t) + \tilde{\mu}(-\varepsilon S, t) - 2\tilde{\mu}(0, \cdot) dt \right] \right\} dS, \\ &= -\frac{\ell J(0, \cdot)}{4\pi} \int_0^{\delta/\varepsilon} \left\{ \left[\frac{S}{(S^2 |y_s(0, \cdot)|^2 + \ell^2)^{3/2}} + O(\varepsilon) \right] \left[\int_0^{\pi} \varepsilon^2 S^2 \tilde{\mu}_{ss}(0, \cdot) + O(\varepsilon^4) dt \right] \right\} dS, \\ &= -\frac{\ell J(0, \cdot)}{4} \int_0^{\delta/\varepsilon} \left\{ \frac{\varepsilon^2 S^3}{(S^2 |y_s(0, \cdot)|^2 + \ell^2)^{3/2}} \left[\frac{1}{\pi} \int_0^{\pi} \tilde{\mu}_{ss}(0, \cdot) dt \right] \right\} dS + O(\varepsilon^2). \end{aligned} \quad (3.8)$$

We find that in the asymptotic limit corresponding to $0 < \varepsilon \ll \delta \ll 1$ that

$$\int_0^{\delta/\varepsilon} \frac{\varepsilon^2 S^3}{(S^2 |y_s(0, \cdot)|^2 + \ell^2)^{3/2}} dS = \delta \frac{\varepsilon}{|y_s(0, \cdot)|^3} + O(\varepsilon^2), \quad (3.9)$$

(recall that $|y_s(0, \cdot)| \neq 0$), and in B, we show that

$$\frac{1}{\pi} \int_0^{\pi} \tilde{\mu}_{ss}(0, \cdot) dt = \frac{1}{2} \Delta_{S^2} \mu(y^*), \quad (3.10)$$

with $\Delta_{S^2} \mu(y^*)$ denoting the spherical Laplacian of μ evaluated at y^* . Thus, we have found that

$$U(y^*; \varepsilon, \delta) = -\delta \frac{\varepsilon \ell J(0, \cdot)}{8 |y_s(0, \cdot)|^3} \Delta_{S^2} \mu(y^*) + O(\varepsilon^2). \quad (3.11)$$

This result gives the leading-order asymptotic behavior for U . The results (3.9) and (3.11) provide the following insights about the close evaluation problem.

- The function that is integrated in (3.9) has a *smooth limit to a finite value* at the north pole. In other words, despite the sharply peaked behavior of the kernel, the leading-order asymptotic behavior of the integrand is smooth.
- Working in a *rotated spherical coordinate system* in which $y^*/|y^*|$ serves as the north pole effectively removes the dependence with respect to the azimuthal angle, denoted here by t , through an *averaging* about the north pole.
- The above procedure provides a way to rewrite the layer potential that avoids the close-evaluation problem.

Similar conclusions can be drawn for the single-layer potential. Using the same parameterization as above, we write (2.10) as

$$v(y^* + \varepsilon \ell n^*) = \frac{1}{4\pi} \int_{-\pi}^{\pi} \int_0^{\pi} G(s, t; \varepsilon) \tilde{\rho}(s, t) \sin(s) ds dt, \quad (3.12)$$

with $\tilde{\rho}(s, t) = \rho(y(s, t))$, and

$$G(s, t; \varepsilon) = \frac{J(s, t)}{|y_d(s, t) + \varepsilon \ell n^*|}. \quad (3.13)$$

Just as we have done for u , we consider the contribution to v made by a small portion of B about $y = y^*$, which we denote by V , defined with the parameter δ as

$$V(y^*; \varepsilon, \delta) = \frac{1}{4\pi} \int_{-\pi}^{\pi} \int_0^{\delta} G(s, t; \varepsilon) \tilde{\rho}(s, t) \sin(s) ds dt. \quad (3.14)$$

Next, we substitute $s = \varepsilon S$ and obtain

$$V(y^*; \varepsilon, \delta) = \frac{1}{4\pi} \int_{-\pi}^{\pi} \int_0^{\delta/\varepsilon} G(\varepsilon S, t; \varepsilon) \tilde{\rho}(\varepsilon S, t) \sin(\varepsilon S) \varepsilon dS dt. \quad (3.15)$$

By expanding G about $\varepsilon = 0$, we find that that

$$G(\varepsilon S, t; \varepsilon) = \frac{1}{\varepsilon} \frac{J(0, \cdot)}{(S^2 |y_s(0, \cdot)|^2 + \ell^2)^{1/2}} + O(1). \quad (3.16)$$

Substituting this leading-order behavior into (3.15) along with $\sin(\varepsilon S) = \varepsilon S + O(\varepsilon^3)$, and $\tilde{\rho}(\varepsilon S, t) = \tilde{\rho}(0, \cdot) + O(\varepsilon)$, and then integrating that result with respect to t , we obtain

$$V(y^*; \varepsilon, \delta) = \frac{J(0, \cdot) \tilde{\rho}(0, \cdot)}{2} \int_0^{\delta/\varepsilon} \left[\frac{\varepsilon S}{(S^2 |y_s(0, \cdot)|^2 + \ell^2)^{1/2}} + O(\varepsilon^2) \right] dS. \quad (3.17)$$

In the asymptotic limit in which $0 < \varepsilon \ll \delta \ll 1$, we find that

$$V(y^*; \varepsilon, \delta) = \delta \frac{J(0, \cdot)}{2 |y_s(0, \cdot)|} \tilde{\rho}(0, \cdot) + O(\varepsilon). \quad (3.18)$$

This result gives the leading-order asymptotic behavior for V .

In light of the asymptotic analysis given above, we have found a natural procedure to compute the close evaluation of layer potentials that avoids the challenges associated with evaluating nearly singular integrals. There are three, crucial steps in this procedure.

1. Rotate the spherical coordinate system so that $y^*/|y^*|$ serves as the north pole where y^* denotes the boundary point at which the kernel for the layer potential is peaked.

2. Integrate first with respect to the azimuthal angle to average the function about the north pole.
3. Integrate the remaining function with respect to the polar angle.

It is important in the third step to integrate with respect to s rather than $z = \cos(s)$, which is often done, because the asymptotic analysis above is explicitly aided by $\sin(s)$ term inherent in the spherical integral.

These results suggest that following these three steps leads to a natural numerical method to evaluate double- and single-layer potentials close to the boundary. The leading-order asymptotic behaviors given by (3.11) and (3.18) show that this method yields an $O(\varepsilon^2)$ error for the modified double-layer potential and an $O(\varepsilon)$ error for the single-layer potential. The smaller error with the modified double-layer potential is due to the subtraction of $\mu(y^*)$ in conjunction with the azimuthal averaging step. Additionally (3.11) and (3.18) provide explicit expressions for the limiting behavior of the double- and single-layer potentials, respectively, as $s \rightarrow 0$. These results may be used in the computation of the integral with respect to the polar angle in the third step. However, we avoid needing these results in the specific method we give below by choosing an open quadrature rule for s that does not require evaluation at the end points of the interval.

4 Numerical method for the close evaluation of double- and single-layer potentials

We now give a numerical method for computing the close evaluation of double- and single-layer potentials by following the three-step procedure given above. Suppose we have parameterized B by $y = y(\theta, \varphi)$ with $\theta \in [0, \pi]$ and $\varphi \in [-\pi, \pi]$ where $y^* = y(\theta^*, \varphi^*)$. We seek to compute

$$I_{3D}(y^*) = \frac{1}{4\pi} \int_{-\pi}^{\pi} \int_0^{\pi} F(\theta, \varphi; \theta^*, \varphi^*) \sin(\theta) d\theta d\varphi, \quad (4.1)$$

where F is nearly singular at $(\theta, \varphi) = (\theta^*, \varphi^*)$. For the modified double-layer potential resulting from applying a subtraction method, we have

$$F(\theta, \varphi; \theta^*, \varphi^*) = \frac{\tilde{n}(\theta, \varphi) \cdot [y(\theta^*, \varphi^*) - y(\theta, \varphi) - \varepsilon \ell \tilde{n}(\theta^*, \varphi^*)]}{|y(\theta^*, \varphi^*) - y(\theta, \varphi) - \varepsilon \ell \tilde{n}(\theta^*, \varphi^*)|^3} J(\theta, \varphi) [\tilde{\mu}(\theta, \varphi) - \tilde{\mu}(\theta^*, \varphi^*)], \quad (4.2)$$

and for the single-layer potential, we have

$$F(\theta, \varphi; \theta^*, \varphi^*) = \frac{J(\theta, \varphi)}{|y(\theta^*, \varphi^*) - y(\theta, \varphi) + \varepsilon \ell \tilde{n}(\theta^*, \varphi^*)|} \tilde{\rho}(\theta, \varphi), \quad (4.3)$$

where $J(\theta, \varphi) = |y_\theta(\theta, \varphi) \times y_\varphi(\theta, \varphi)| / \sin \theta$.

Motivated by the local analysis leading to (3.11) and (3.18) above, we perform the following three-step procedure to numerically evaluate $I_{3D}(y^*)$.

1. Rotate this integral to another spherical coordinate system whose north pole is aligned with $y^*/|y^*|$. The details of this rotation are given in A, and lead to $\theta = \theta(s, t)$ and $\varphi = \varphi(s, t)$ with $s \in [0, \pi]$ and $t \in [-\pi, \pi]$ where $\theta(0, \cdot) = \theta^*$ and $\varphi(0, \cdot) = \varphi^*$. Upon applying this rotation, we obtain the spherical integral

$$I_{3D}(y^*) = \frac{1}{4\pi} \int_{-\pi}^{\pi} \int_0^{\pi} \tilde{F}(s, t) \sin(s) ds dt, \quad (4.4)$$

with $\tilde{F}(s, t) = F(\theta(s, t), \varphi(s, t); \theta^*, \varphi^*)$.

2. Use the $2N$ -point Periodic Trapezoid Rule to compute

$$\frac{1}{2\pi} \int_{-\pi}^{\pi} \tilde{F}(s, t) dt = \bar{F}(s) \approx \bar{F}^N(s) = \frac{1}{2N} \sum_{j=1}^{2N} \tilde{F}(s, t_j), \quad (4.5)$$

with $t_j = -\pi + \pi(j-1)/N$ for $j = 1, \dots, 2N$.

3. Use the N -point Gauss-Legendre quadrature rule to compute the integral in s . Let $z_i \in (-1, 1)$ for $i = 1, \dots, N$ denote the Gauss-Legendre quadrature points with corresponding weights w_i . We map the quadrature points according to $s_i = \pi(z_i + 1)/2$ to the interval $(0, \pi)$ and compute the numerical approximation,

$$I_{3D} \approx I_{3D}^N = \frac{\pi}{4} \sum_{i=1}^N \bar{F}^N(s_i) \sin(s_i) w_i. \quad (4.6)$$

In the first step of the procedure, the coordinate system is rotated so that (θ^*, φ^*) corresponds to the north pole of the spherical coordinate system. This rotation sets up the second step, which computes the azimuthal average of the function with respect to t about the north pole. The factor of $1/(2\pi)$ is incorporated into this step to explicitly obtain an averaging operation yielding $\bar{F}^N(s)$, which is a smooth function in the polar angle, s . For the third step, we have chosen to use the Gauss-Legendre quadrature rule for which the quadrature points satisfy $0 < s_1 < s_2 < \dots < s_N < \pi$. Consequently, we do not need to explicitly evaluate $\bar{F}^N(0)$. Alternatively, we could have chosen a closed rule that includes the end points. For that case, we would use (3.11) and (3.18) to explicitly prescribe the needed values in the limit as $s \rightarrow 0$.

This numerical method is based on the product Gaussian quadrature rule for spherical integrals [3]. That quadrature rule uses a $2N$ -point Periodic Trapezoid Rule in the azimuthal angle and N -point Gauss-Legendre quadrature rule in the cosine of the polar angle, $z = \cos(s) \in [-1, 1]$. However, the results of the local analysis above show that integrating with respect to the polar angle, s , is better since the factor of $\sin(s)$ plays an important role in the asymptotic behavior. Thus, rather than transforming (4.1) by substituting $z = \cos(s)$, we map the Gauss-Legendre quadrature rule from $[-1, 1]$ to $[0, \pi]$ using $s_i = \pi(z_i + 1)/2$ for $i = 1, \dots, N$. Consequently, the mapped quadrature weights are $\pi w_j/2$, which is accounted for in (4.6) by the $\pi/4$ factor. We show in the numerical results presented in Section 6 that this subtle and seemingly small change to the product Gaussian quadrature rule is significant and yields substantially better results.

Provided that the densities, μ and ρ , for the double- and single-layer potentials, respectively, are known to very high accuracy, the main cause of numerical error for the close evaluation problem is due to the sharp peak of the kernels about $y = y^*$. For that case, the leading-order asymptotic expansions given by (3.11) and (3.18) indicate that this numerical method yields an $O(\varepsilon^2)$ error for the modified double-layer potential and an $O(\varepsilon)$ error for the single-layer potential, respectively. These asymptotic error estimates are valid only when the value of N used in this numerical method is sufficiently large to resolve the density and the boundary. Otherwise, errors introduced by inaccuracy of the density and/or under-resolution of the boundary will dominate over these asymptotic error estimates.

5 Numerical solution of the boundary integral equations

The numerical method described above can also be used to solve the boundary integral equations for the densities, (2.3) and (2.6). We describe its use in the context of the Galerkin method [4, 5, 6, 7]. As we have done above, we suppose that we have parameterized B by $y = y(\theta, \varphi)$ with $\theta \in [0, \pi]$ and $\varphi \in [-\pi, \pi]$.

To compute the density, μ , for the double-layer potential, we write (2.3) compactly as

$$-\frac{1}{2}\mu + \mathcal{K}_D[\mu] = f. \quad (5.1)$$

We introduce the approximation for μ ,

$$\mu(y(\theta, \varphi)) = \tilde{\mu}(\theta, \varphi) \approx \sum_{n=0}^{N-1} \sum_{m=-n}^n Y_{nm}(\theta, \varphi) \hat{\mu}_{nm}, \quad (5.2)$$

with $\{Y_{nm}(\theta, \varphi)\}$ denoting the orthonormal set of spherical harmonics. Note that N in (5.2) corresponds also to the order of the quadrature rule detailed in Section 4 so that the order of this approximation is commensurate with the order of the quadrature rule to be used. Substituting (5.2) into (5.1) and taking the inner product with $Y_{n'm'}(\theta^*, \varphi^*)$, we obtain the Galerkin equations,

$$-\frac{1}{2} \hat{\mu}_{n'm'} + \sum_{n=0}^{N-1} \sum_{m=-n}^n \langle Y_{n'm'}, \mathcal{K}_D[Y_{nm}] \rangle \hat{\mu}_{nm} = \langle Y_{n'm'}, f \rangle, \quad (5.3)$$

with

$$\mathcal{K}_D[Y_{nm}](\theta^*, \varphi^*) = \frac{1}{4\pi} \int_{-\pi}^{\pi} \int_0^{\pi} \left[\frac{\tilde{n}(\theta, \varphi) \cdot (y(\theta^*, \varphi^*) - y(\theta, \varphi))}{|y(\theta^*, \varphi^*) - y(\theta, \varphi)|^3} J(\theta, \varphi) \sin(\theta) \right] Y_{nm}(\theta, \varphi) d\theta d\varphi. \quad (5.4)$$

We construct the $N^2 \times N^2$ linear system for the unknown coefficients, $\hat{\mu}_{n'm'}$ resulting from (5.3) evaluated for $n' = 0, \dots, N-1$ with corresponding values of m' . To evaluate (5.4), we use (2.8) to rewrite it as

$$\begin{aligned} \mathcal{K}_D[Y_{nm}](\theta^*, \varphi^*) &= -\frac{1}{2} Y_{nm}(\theta^*, \varphi^*) \\ &+ \frac{1}{4\pi} \int_{-\pi}^{\pi} \int_0^{\pi} \left[\frac{\tilde{n}(\theta, \varphi) \cdot (y(\theta^*, \varphi^*) - y(\theta, \varphi))}{|y(\theta^*, \varphi^*) - y(\theta, \varphi)|^3} J(\theta, \varphi) \sin(\theta) \right] [Y_{nm}(\theta, \varphi) - Y_{nm}(\theta^*, \varphi^*)] d\theta d\varphi, \end{aligned} \quad (5.5)$$

and evaluate the integral in this expression using the numerical method described above. To compute the inner products, $\langle Y_{n'm'}, \mathcal{K}_D[Y_{nm}] \rangle$ and $\langle Y_{n'm'}, f \rangle$, we use the product Gaussian quadrature rule for spherical integrals [3] with N Gauss-Legendre quadrature points and $2N$ Periodic Trapezoid Rule points.

To compute the density ρ for the single-layer potential, we write (2.6) compactly as

$$\frac{1}{2} \rho - \mathcal{K}_S[\rho] = g. \quad (5.6)$$

We introduce the approximation for ρ ,

$$\rho(y(\theta, \varphi)) = \tilde{\rho}(\theta, \varphi) \approx \sum_{n=0}^{N-1} \sum_{m=-n}^n Y_{nm}(\theta, \varphi) \hat{\rho}_{nm}. \quad (5.7)$$

Performing the same calculations as above, we find that $\hat{\rho}_{nm}$ satisfies the Galerkin equations,

$$\frac{1}{2} \hat{\rho}_{n'm'} - \sum_{n=0}^{N-1} \sum_{m=-n}^n \langle \mathcal{K}_S^\dagger[Y_{n'm'}], Y_{nm} \rangle \hat{\rho}_{nm} = \langle Y_{n'm'}, g \rangle, \quad (5.8)$$

where \mathcal{K}_S^\dagger denotes the adjoint of \mathcal{K}_S defined according to

$$\mathcal{K}_S^\dagger[Y_{n'm'}](\theta, \varphi) = \frac{1}{4\pi} \int_{-\pi}^{\pi} \int_0^{\pi} \left[\frac{\tilde{n}(\theta^*, \varphi^*) \cdot (y(\theta^*, \varphi^*) - y(\theta, \varphi))}{|y(\theta^*, \varphi^*) - y(\theta, \varphi)|^3} J(\theta^*, \varphi^*) \sin(\theta^*) \right] Y_{n'm'}(\theta^*, \varphi^*) d\theta^* d\varphi^*. \quad (5.9)$$

Recall that $\tilde{n}(\theta^*, \varphi^*)$ is the unit normal pointing out of D . For this integral, we use (2.8) to write

$$\begin{aligned} \mathcal{K}_S^\dagger[Y_{n'm'}](\theta, \varphi) &= -\frac{1}{2}Y_{n'm'}(\theta, \varphi) \\ &+ \frac{1}{4\pi} \int_{-\pi}^{\pi} \int_0^{\pi} \left[\frac{\tilde{n}(\theta^*, \varphi^*) \cdot (y(\theta^*, \varphi^*) - y(\theta, \varphi))}{|y(\theta^*, \varphi^*) - y(\theta, \varphi)|^3} J(\theta^*, \varphi^*) \sin(\theta^*) \right] [Y_{n'm'}(\theta^*, \varphi^*) - Y_{n'm'}(\theta, \varphi)] d\theta^* d\varphi^*, \end{aligned} \quad (5.10)$$

which we then compute using the numerical method described above. We use the product Gaussian quadrature rule with N Gauss-Legendre quadrature points and $2N$ Periodic Trapezoid Rule points to compute the remaining inner products, $\langle \mathcal{K}_S^\dagger Y_{n'm'}, Y_{nm} \rangle$ and $\langle Y_{n'm'}, g \rangle$, needed to form the $N^2 \times N^2$ linear system for the unknown coefficients, $\hat{\rho}_{n'm'}$ for $n' = 0, \dots, N-1$ and corresponding values of m' .

6 Numerical results

We present numerical results for computing the close evaluation of double- and single-layer potentials using the method detailed in Section 4. For the double-layer potential examples discussed in Section 6.1 below, we have computed the density, $\tilde{\mu}$, by solving boundary integral equation (5.1) using the Galerkin method discussed in Section 5. Then, we compute the double-layer potential using that density for two ellipsoids and study the error. In Section 6.2 below, we compute the representation formula for a harmonic function given as the difference between the double- and single-layer potentials using densities that are known exactly. We study the error in computing this representation formula in two different domains and evaluate those results.

6.1 Double-layer potential

We present results in computing the solution of the interior Dirichlet problem (2.1) for two different ellipsoids. For all of these examples, we set the harmonic function,

$$u_{\text{ex}}(x) = |x - x_0|^{-1}, \quad x \in D, \quad (6.1)$$

with $x_0 \in E$ to be the exact solution. Therefore, we prescribe

$$f(y) = |y - x_0|^{-1}, \quad y \in B, \quad (6.2)$$

as the Dirichlet boundary data.

With the boundary data given in (6.2), we first use the Galerkin method described in Section 5 to solve for $\hat{\mu}_{nm}$, the expansion coefficients for the density introduced in (5.2). We then use (5.2) to evaluate the density, $\tilde{\mu}$, that is needed for computing the double-layer potential. To test our method for close evaluation points, we evaluate the double-layer potential at the points $x = y^* - \varepsilon n^*$ (we have set $\ell = 1$) for various points y^* on the boundary of the domain and for various ε . The error is determined by computing the absolute value of the difference between the double-layer potential result and the exact harmonic function, $u_{\text{ex}}(y^* - \varepsilon n^*) = |y^* - \varepsilon n^* - x_0|^{-1}$. We show error results for computing $u(x)$ over a range of ε values spanning several orders of magnitude using four different methods listed below using the kernel, K defined in (3.2).

Method 1: Compute

$$u(y^* - \varepsilon n^*) = \frac{1}{4\pi} \int_{-\pi}^{\pi} \int_{-1}^1 K(\cos^{-1}(z), t; \varepsilon) \tilde{\mu}(\cos^{-1}(z), t) dz dt$$

using an N -point Gauss-Legendre quadrature rule for $z \in [-1, 1]$ and a $2N$ Periodic Trapezoid Rule for $t \in [-\pi, \pi]$.

Method 2: Compute

$$u(y^* - \varepsilon n^*) = \frac{1}{4\pi} \int_{-\pi}^{\pi} \int_0^{\pi} K(s, t; \varepsilon) \tilde{\mu}(s, t) \sin(s) ds dt$$

using an N -point Gauss-Legendre quadrature rule for $s \in [0, \pi]$ and a $2N$ Periodic Trapezoid Rule for $t \in [-\pi, \pi]$.

Method 3: Compute

$$u(y^* - \varepsilon n^*) = -\tilde{\mu}(0, \cdot) + \frac{1}{4\pi} \int_{-\pi}^{\pi} \int_{-1}^1 K(\cos^{-1}(z), t; \varepsilon) [\tilde{\mu}(\cos^{-1}(z), t) - \tilde{\mu}(0, \cdot)] dz dt$$

using an N -point Gauss-Legendre quadrature rule for $z \in [-1, 1]$ and a $2N$ Periodic Trapezoid Rule for $t \in [-\pi, \pi]$.

Method 4: Compute

$$u(y^* - \varepsilon n^*) = -\tilde{\mu}(0, \cdot) + \frac{1}{4\pi} \int_{-\pi}^{\pi} \int_0^{\pi} K(s, t; \varepsilon) [\tilde{\mu}(s, t) - \tilde{\mu}(0, \cdot)] \sin(s) ds dt$$

using an N -point Gauss-Legendre quadrature rule for $s \in [0, \pi]$ and a $2N$ Periodic Trapezoid Rule for $t \in [-\pi, \pi]$.

For each of these methods, we have applied the rotation of the coordinate system described as the first step in the procedure detailed in Section 4. Methods 1 and 2 compute the double-layer potential given by (2.2) directly and integrate with respect to $z = \cos(s)$ and s , respectively. Methods 3 and 4 use the subtraction method, so they compute the modified double-layer potential given in (2.9). Method 3 integrates with respect to $z = \cos(s)$ and Method 4 integrates with respect to s . Method 4 is the one we have proposed here to compute the close-evaluation of the double-layer potential.

In the examples that follow, we consider two different ellipsoids used by Atkinson [4]. Let (x_1, x_2, x_3) denote an ordered triple in a Cartesian coordinate system. The boundaries for these ellipsoids are given by

$$y(\theta, \varphi) = (\alpha \sin \theta \cos \varphi, \beta \sin \theta \sin \varphi, \gamma \cos \theta), \quad \theta \in [0, \pi], \quad \varphi \in [-\pi, \pi]. \quad (6.3)$$

For the first example, we set $\alpha = 1$, $\beta = 1.5$, and $\gamma = 2$, and for the second example, we set $\alpha = 1$, $\beta = 2$, and $\gamma = 5$. These two ellipsoids, which we call Ellipsoids 1 and 2, are shown as the left and right plots in Fig. 2, respectively. For both of these examples, we have set $x_0 = (5, 4, 3) \in E$ in (6.1) and (6.2). In Fig. 2 we also identify two boundary points, labeled A and B, lying on the x_1x_3 -plane and the x_1x_2 -plane, respectively, which we will refer to below when we discuss the error results. The coordinates for these points are A = $(-1.16, -0.64, 0)$ and B = $(-0.72, 0, 1.75)$ for Ellipsoid 1, and A = $(-0.74, -0.93, 0)$ and B = $(-1.81, 0, 2.13)$ for Ellipsoid 2.

We have used the Galerkin method with $N = 48$ to compute the density, $\tilde{\mu}$. For Ellipsoid 1 shown in the left plot of Fig. 2, we find that this order resolves $\tilde{\mu}$ with an estimated truncation error on the order of 10^{-15} . Ellipsoid 2 shown in the right plot of Fig. 2 is more elongated along the x_3 axis, so it deviates farther from a sphere than Ellipsoid 1. As a result, we find that the Galerkin method with $N = 48$ yields a larger estimated truncation error for $\tilde{\mu}$ on the order of 10^{-12} . We have subsequently used $N = 48$ in the quadrature rules for the four methods given above.

6.1.1 Results for Ellipsoid 1

In the top row of Fig. 3, we plot \log_{10} of the error made using Method 1. The left two plots show the error over the vertical x_1x_3 -plane and a close-up of the small region near the boundary point, A = $(-1.16, -0.64, 0)$. The right two plots show the error over the horizontal x_1x_2 -plane and a close-up

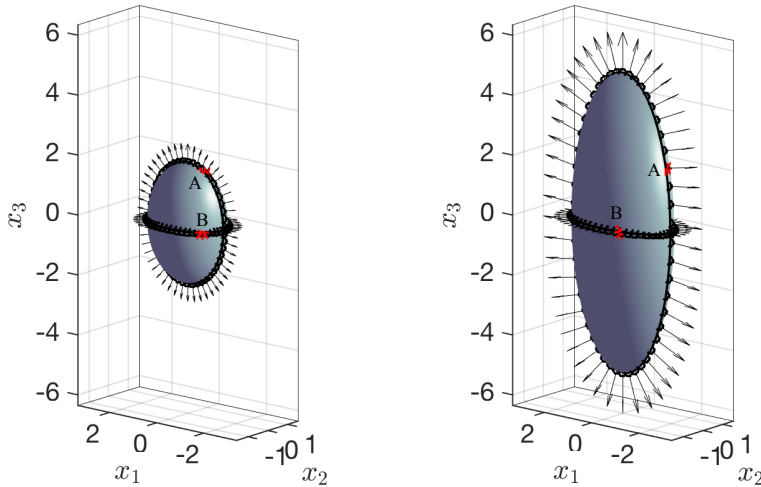


Figure 2: (Left) Boundary surface of the ellipsoid given by (6.3) with $\alpha = 1$, $\beta = 1.5$, and $\gamma = 2$ which we call Ellipsoid 1. (Right) Boundary surface of the ellipsoid given by (6.3) with $\alpha = 1$, $\beta = 2$, and $\gamma = 5$, which we call Ellipsoid 2. In each figure, the two black curves indicate where the boundary of the ellipsoid intersects with the vertical x_1x_3 -plane, and the horizontal x_1x_2 -plane, and the black arrows give the unit outward normal vectors on those curves. The two boundary points labeled A and B lying on the x_1x_3 -plane and x_1x_2 -plane, respectively, give the locations where we investigate the error made by four different methods. The coordinates for these points are $A = (-1.16, -0.64, 0)$ and $B = (-0.72, 0, 1.75)$ in the left plot, and $A = (-0.74, -0.93, 0)$ and $B = (-1.81, 0, 2.13)$ in the right plot.

of the small region near the boundary point, $B = (-0.72, 0, 1.75)$. The bottom row of Fig. 3 shows the same plots for Method 4.

These results show that using Method 1 leads to an $O(1)$ error close to the boundary which is symptomatic of the close evaluation problem. In contrast, the results using Method 4 show an error that is several orders of magnitude smaller. To examine this error more closely, we show in Fig. 4 errors using Methods 1, 2, 3, and 4 evaluated along the normal at point $A = (-1.16, -0.64, 0)$ on the boundary and the x_1x_3 -plane, and at point $B = (-0.72, 0, 1.75)$ on the boundary and the x_1x_2 -plane. In this way, we clearly observe that the subtraction method used in Method 3 and Method 4 leads to substantially smaller errors compared with those made using Method 1 and Method 2. The error for Methods 1, 2, and 3 all appear to asymptote to a fixed value as $\varepsilon \rightarrow 0$. In contrast, we see that the error for Method 4 decreases as $\varepsilon \rightarrow 0$. To study the asymptotic behavior of the error for Method 4, we compute the best linear fit to the error (see dashed black lines in Fig. 4) for the four smallest ε values. These linear fits have slopes of 1.73 for point A and 1.83 for point B consistent with the $O(\varepsilon^2)$ error estimate from the asymptotic analysis in (3.11).

6.1.2 Results for Ellipsoid 2

The error results for Ellipsoid 2 plotted in Figs. 5 and 6 are of the same format as those for Ellipsoid 1 in Figs. 3 and 4, respectively. The close-ups in Fig. 5 show small regions near the boundary points $A = (-0.74, -0.93, 0)$ and $B = (-1.81, 0, 2.13)$.

Figure 5 shows that the error for Method 4 is again several orders of magnitude smaller than that for Method 1. However, the magnitude of the errors appears to be larger for both methods than the previous example. This is due to the larger truncation error associated with the Galerkin method.

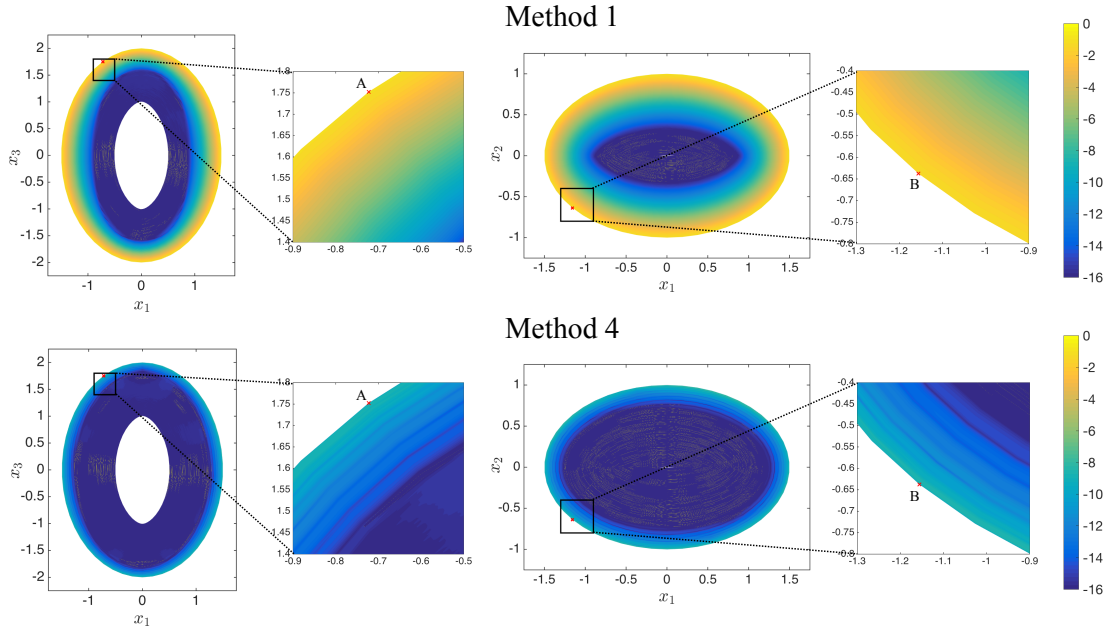


Figure 3: The errors made by Method 1 (top row) and Method 4 (bottom row) for Ellipsoid 1. The first and second columns show \log_{10} of the errors made by these two methods in the x_1x_3 -plane, with the plots in the second column showing a close-up in the vicinity of point A = $(-1.16, -0.64, 0)$. The third and fourth columns show \log_{10} of the errors made by these two methods in the x_1x_2 -plane, with the plots in the fourth column showing a close-up in the vicinity of point B = $(-0.72, 0, 1.75)$.

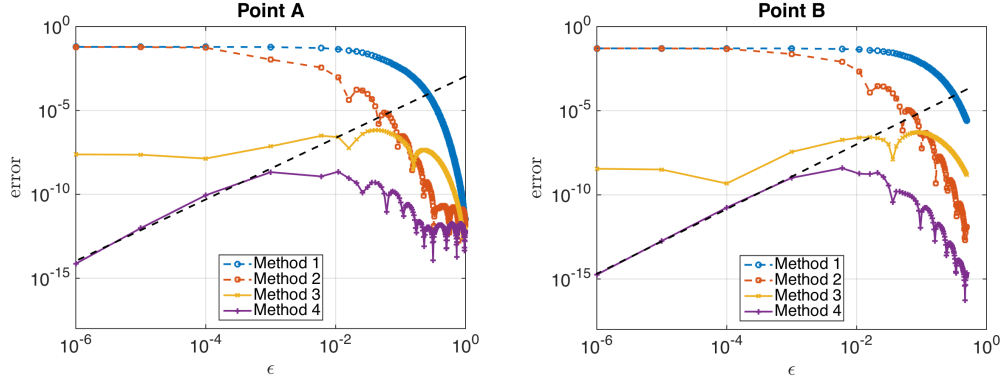


Figure 4: Comparison of errors made by Methods 1 – 4 for Ellipsoid 1 for evaluation points along the normal at distance ε from point A = $(-1.16, -0.64, 0)$ on the boundary and in the x_1x_3 -plane (left plot) and for evaluation points along the normal at distance ε from point B = $(-0.72, 0, 1.75)$ on the boundary and in the x_1x_2 -plane (right plot). The dashed black lines show the best linear fit through the Method 4 errors for the four smallest ε values. Both fits are consistent with the $O(\varepsilon^2)$ asymptotic error estimate given by (3.11).

In Fig. 6, we see that Method 4 clearly has the smallest error. The dashed black lines show the best linear fit to the errors for the four smallest ε values. These linear fits have slopes of 1.83 for point A and 1.92 for point B consistent with $O(\varepsilon^2)$ error estimate in (3.11).

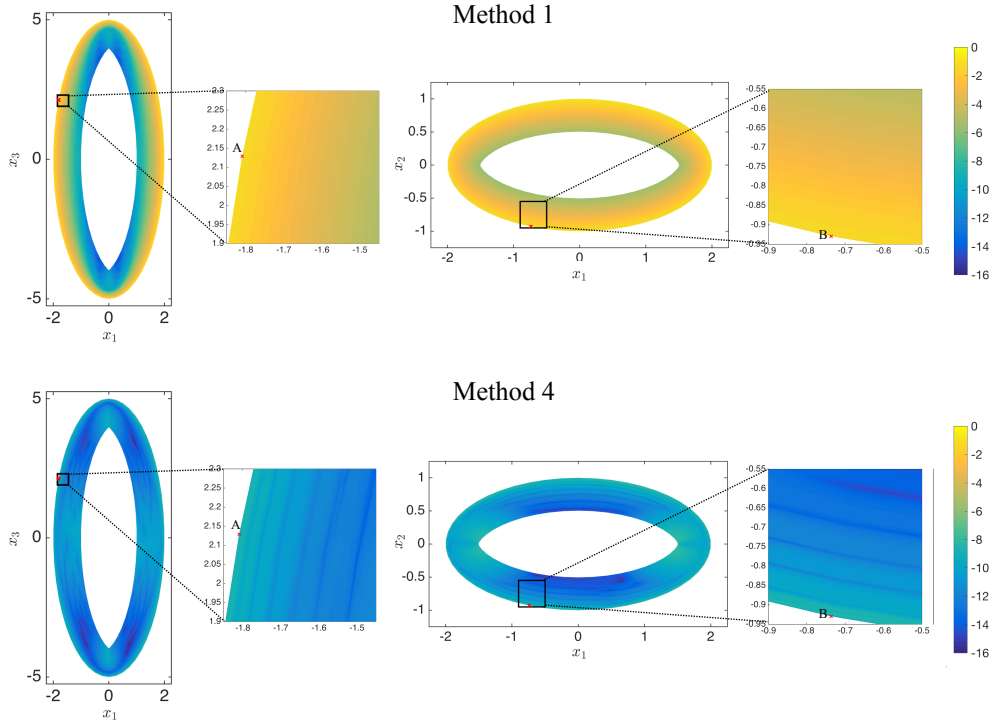


Figure 5: The errors made by Method 1 (top row) and Method 4 (bottom row) for Ellipsoid 2. The first and second columns show \log_{10} of the errors made by these two methods in the x_1x_3 -plane with the plots in the second column showing a close-up in the vicinity of point $A = (-0.74, -0.93, 0)$. The third and fourth columns show \log_{10} of the errors made by these two methods in the x_1x_2 -plane with the plots in the fourth column showing a close-up in the vicinity of point $B = (-1.81, 0, 2.13)$.

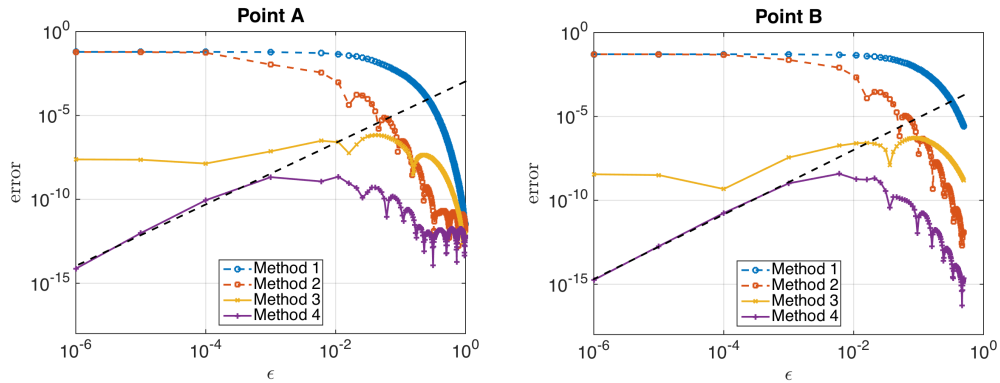


Figure 6: Comparison of errors made by Methods 1 – 4 for Ellipsoid 2 for evaluation points along the normal at distance ε from point $A = (-0.74, -0.93, 0)$ on the boundary and in the x_1x_3 -plane (left plot) and for evaluation points along the normal at distance ε from point $B = (-1.81, 0, 2.13)$ on the boundary and in the x_1x_2 -plane (right plot). The dashed, black lines show the best linear fit through the Method 4 errors for the four smallest ε values. Both fits are consistent with the $O(\varepsilon^2)$ asymptotic error estimate given by (3.11).

6.1.3 Summary of double-layer potential results

For both Ellipsoids 1 and 2, we have observed that Method 4 provides the most accurate evaluation of the double-layer potential for close evaluation points. Method 3 is the next most accurate. However, the errors for Methods 1, 2, and 3 all appear to asymptote to a finite value rather than decay to zero as the error for Method 4 does. For this reason, we conclude that Method 4 is an effective method for the close evaluation of the double-layer potential.

The errors for Method 4 plotted in Figs. 4 and 6 show a characteristic behavior. For very small values of ε corresponding to points very close to the boundary, Method 4 is highly accurate with an error approaching machine precision. For intermediate values of ε , the error obtained with Method 4 increases as the value of ε starts to coincide with the spacing of the Gauss-Legendre quadrature points in the polar angle s . For bigger values of ε , Methods 1, 2, 3, and 4 have errors of a similar order of magnitude because the evaluation point is far enough from the boundary that the double-layer potential is no longer nearly singular.

6.2 The representation formula

When the truncation error for the Galerkin method is not sufficiently small, it dominates over the asymptotic error for the close evaluation of the double-layer potential given by (3.11) and the single-layer potential given by (3.18). For the exterior Neumann problem, (2.4), boundary data are in terms of the gradient of a harmonic function. Consequently, those boundary data tend to be less smooth than those for the interior Dirichlet problem. Because of this, the Galerkin method to solve boundary integral equation (5.6) for a boundary that deviates significantly from a sphere requires N in (5.7) to be sufficiently large that the truncation error does not interfere with the $O(\varepsilon)$ asymptotic error estimate for the single-layer potential. It is in this way that the Galerkin method is a limitation and another high-order method can be used to compute the densities for the double- and single-layer potentials for more general domains [11].

The focus of this paper is in the close evaluation problem. Thus, we consider an alternate example to test the asymptotic error estimates for the double- and single-layer potentials rather than consider another high-order method to solve weakly singular boundary integral equations for the densities. Consider the representation formula for a harmonic function in domain D with boundary B ,

$$u(x) = \frac{1}{4\pi} \int_B \left[\frac{1}{|x-y|} n(y) \cdot \nabla u(y) - \frac{n(y) \cdot (x-y)}{|x-y|^3} u(y) \right] d\sigma_y, \quad x \in D. \quad (6.4)$$

Given a prescribed harmonic function u and its normal derivative on B , (6.4) gives a formula for computing $u(x)$ for any $x \in D$ in terms of the difference between the single- and double-layer potentials, where the prescribed boundary data can be interpreted as the corresponding densities, ρ and μ . For this case there is no boundary integral equation to solve since the densities are known exactly.

For the following examples, we have set the harmonic function

$$u_{\text{ex}}(x_1, x_2, x_3) = e^{x_3} (\sin x_1 + \sin x_2), \quad (6.5)$$

following Beale *et al.* [10], to be the exact solution. We set (6.5) on the boundary to be μ and its normal derivative on the boundary to be ρ , which are used in the double- and single-layer potentials, respectively, to evaluate (6.4). For the following examples, we use the four methods described below.

Method 1: Compute

$$u(y^* - \varepsilon n^*) = \frac{1}{4\pi} \int_{-\pi}^{\pi} \int_{-1}^1 [G(\cos^{-1}(z), t; \varepsilon) \tilde{\rho}(\cos^{-1}(z), t) - K(\cos^{-1}(z), t; \varepsilon) \tilde{\mu}(\cos^{-1}(z), t)] dz dt$$

using an N -point Gauss-Legendre quadrature rule for $z \in [-1, 1]$, and a $2N$ Periodic Trapezoid Rule for $t \in [-\pi, \pi]$.

Method 2: Compute

$$u(y^* - \varepsilon n^*) = \frac{1}{4\pi} \int_{-\pi}^{\pi} \int_0^{\pi} [G(s, t; \varepsilon) \tilde{\rho}(s, t) - K(s, t; \varepsilon) \tilde{\mu}(s, t)] \sin(s) ds dt$$

using an N -point Gauss-Legendre quadrature rule for $s \in [0, \pi]$, and a $2N$ Periodic Trapezoid Rule for $t \in [-\pi, \pi]$.

Method 3: Compute

$$u(y^* - \varepsilon n^*) = \tilde{\mu}(0, \cdot) + \frac{1}{4\pi} \int_{-\pi}^{\pi} \int_{-1}^1 [G(s, t; \varepsilon) \tilde{\rho}(\cos^{-1}(z), t) - K(\cos^{-1}(z), t; \varepsilon) [\tilde{\mu}(\cos^{-1}(z), t) - \tilde{\mu}(0, \cdot)]] dz dt$$

using an N -point Gauss-Legendre quadrature rule for $z \in [-1, 1]$, and a $2N$ Periodic Trapezoid Rule for $t \in [-\pi, \pi]$.

Method 4: Compute

$$u(y^* - \varepsilon n^*) = \tilde{\mu}(0, \cdot) + \frac{1}{4\pi} \int_{-\pi}^{\pi} \int_0^{\pi} [G(s, t; \varepsilon) \tilde{\rho}(s, t) - K(s, t; \varepsilon) [\tilde{\mu}(s, t) - \tilde{\mu}(0, \cdot)]] \sin(s) ds dt$$

using an N -point Gauss-Legendre quadrature rule for $s \in [0, \pi]$, and a $2N$ Periodic Trapezoid Rule for $t \in [-\pi, \pi]$.

Here, K is the kernel defined in (3.2) and G is the kernel defined in (3.13).

Those four methods are a combination of the four methods used in Section 6.1 for the double-layer potential, and the corresponding evaluation of the single-layer potential. Methods 1 and 2 do not use the subtraction method for the double-layer potential, and Methods 3 and 4 use the subtraction method. Methods 1 and 3 integrate with respect to $z = \cos(s)$, and Methods 2 and 4 integrate with respect to s . According to the asymptotic error estimates given by (3.11) and (3.18), we expect Method 4 to exhibit an $O(\varepsilon)$ error in evaluating (6.4).

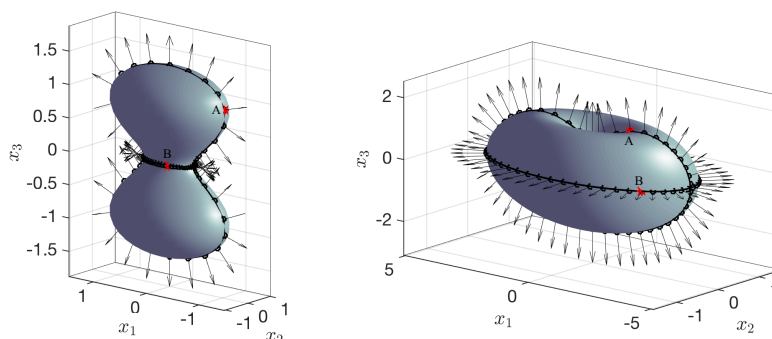


Figure 7: (Left) Boundary surface of the peanut-shaped domain given by (6.6) with $R(\theta)$ given by (6.7). (Right) Boundary surface of the inverted mushroom cap domain given by (6.6) with $R(\theta)$ given by (6.8). In both domains, the two black curves indicate where the boundary intersects with the vertical x_1x_3 -plane, and the horizontal x_1x_2 -plane, and the black arrows give the unit outward normal vectors on those curves. The two boundary points labeled A and B lying on the x_1x_3 -plane and x_1x_2 -plane, respectively, give the locations where we investigate the error made by four different methods. For the peanut-shaped domain, $A = (-0.16, -0.21, 0)$ and $B = (-1.04, 0, 0.94)$, and for the inverted mushroom cap, $A = (-3.07, -1.27, 0)$ and $B = (-1.55, 0, 1.41)$.

In the examples that follow, we consider two domains used by Atkinson [4, 5]. The boundaries for these two domains are given by

$$y(\theta, \varphi) = R(\theta)(\sin \theta \cos \varphi, 2 \sin \theta \sin \varphi, \cos \theta), \quad \theta \in [0, \pi], \quad \varphi \in [-\pi, \pi]. \quad (6.6)$$

For the first example, which resembles a peanut, we have set

$$R(\theta) = \sqrt{\cos 2\theta + \sqrt{1.1 - \sin^2 2\theta}}. \quad (6.7)$$

For the second example, which resembles an inverted mushroom cap, we have set

$$R(\theta) = 2 - \frac{1}{1 + 100(1 - \cos \theta)}. \quad (6.8)$$

The peanut and inverted mushroom cap domains are shown as the left and right plots in Fig. 7, respectively. In Fig. 7, we identify two boundary points, labeled A and B, lying on the x_1x_3 -plane and the x_1x_2 -plane, respectively. For the peanut, $A = (-0.16, -0.21, 0)$ and $B = (-1.04, 0, 0.94)$. For the inverted mushroom cap, $A = (-3.07, -1.27, 0)$ and $B = (-1.55, 0, 1.41)$. We refer to these points below when we discuss the error results.

Since we use exact densities, we are more easily able to use highly resolved computations for these two examples. For the peanut domain, we have set $N = 120$ and for the inverted mushroom cap, we have set $N = 80$.

6.2.1 Results for peanut-shaped domain

The error results plotted in Figs. 8 and 9 are the same format as those in Figs. 3 and 4, respectively. Just like those for the double-layer potential, the results in Fig. 8 clearly show that the error for Method 4 is several orders of magnitude smaller than that for Method 1. Moreover, Fig. 9 shows that Methods 3 and 4 have significantly smaller errors than Methods 1 and 2 demonstrating that using the modified double-layer potential resulting from applying the subtraction method is effective. These errors show that Methods 1, 2, and 3 asymptote to a fixed value as $\varepsilon \rightarrow 0$. In contrast, the error for Method 4 decreases as $\varepsilon \rightarrow 0$. To study the asymptotic behavior of the error for Method 4, we compute the best linear fit to the error (see dashed black lines in Fig. 9) for the four smallest ε values along the normal for two chosen points, A and B. These linear fits have slopes of 1.00 for point A and 1.01 for point B consistent with the expected $O(\varepsilon)$ error estimate.

6.2.2 Results for inverted mushroom cap domain

The error results plotted in Figs. 10 and 11 are the same format as those in Figs. 8 and 9, respectively. Fig. 10 also shows that Method 4 clearly outperforms Method 1. Fig. 11 shows that the subtraction method used for Methods 3 and 4 yields much better results compared with those for Methods 1 and 2. Again, Methods 1, 2, and 3 all appear to asymptote to a fixed value as $\varepsilon \rightarrow 0$, where Method 4 decreases. The dashed black lines in Fig. 11 show the best linear fits to the error for Method 4 for the four smallest ε values. The slopes of these linear fits are 1.01 for point A and 1.00 for point B consistent with the expected $O(\varepsilon)$ error estimate given by (3.18).

6.2.3 Summary of representation formula results

For both the peanut and inverted mushroom cap domains, we have observed that Method 4 provides the most accurate evaluation of the representation formula for close evaluation points. Method 3 is the next most accurate due to the use of the subtraction method. The errors of Methods 1, 2, and 3 all asymptote to a finite value as $\varepsilon \rightarrow 0$, whereas the error for Method 4 decays to zero as $O(\varepsilon)$. For this reason, we conclude that Method 4 is effective for the close evaluation of the representation formula. The error for Method 4 demonstrates the same characteristic behavior discussed for the double-layer

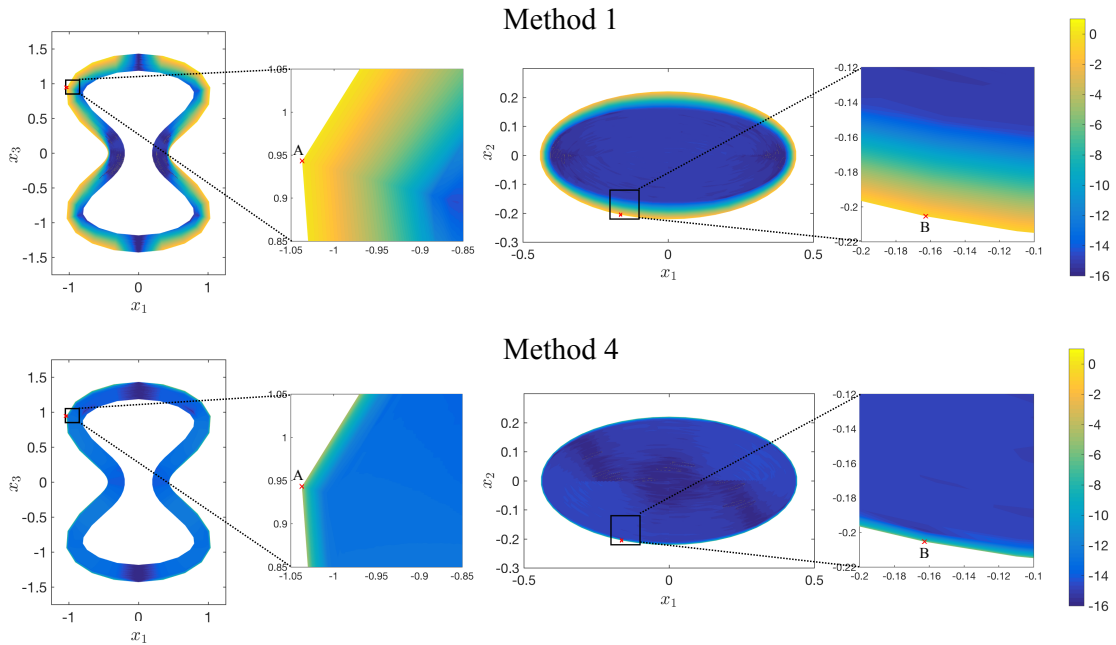


Figure 8: The errors made by Method 1 (top row) and Method 4 (bottom row) for the peanut-shaped domain shown on the left plot of Fig. 8. The first and second columns show \log_{10} of the errors made by these two methods in the x_1x_3 -plane with the plots in the second column showing a close-up in the vicinity of point A = $(-0.16, -0.21, 0)$. The third and fourth columns show \log_{10} of the errors made by these two methods in the x_1x_2 -plane with the plots in the fourth column showing a close-up in the vicinity of point B = $(-1.04, 0, 0.94)$.

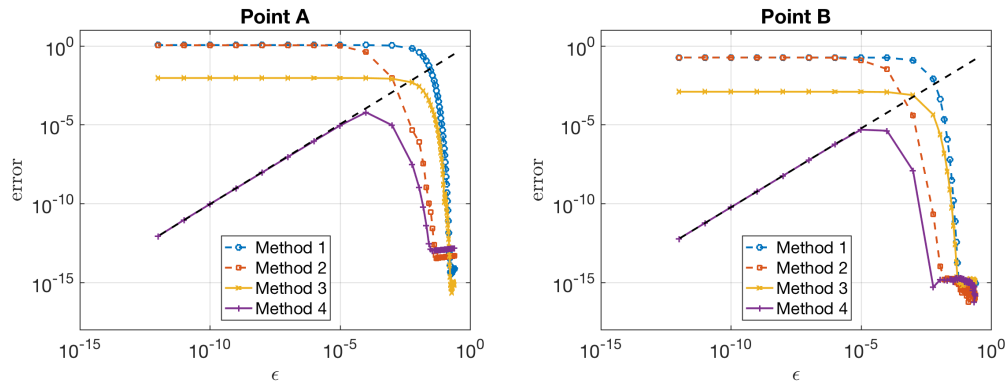


Figure 9: Comparison of errors made by Methods 1 – 4 for the peanut-shaped domain for evaluation points along the normal at distance ε from point A = $(-0.16, -0.21, 0)$ on the boundary and in the x_1x_3 -plane (left plot) and for evaluation points along the normal at distance ε from point B = $(-1.04, 0, 0.94)$ on the boundary and in the x_1x_2 -plane (right plot). The dashed, black lines show the best linear fit through the Method 4 errors for the four smallest ε values. For both fits, the slopes are consistent with the $O(\varepsilon)$ asymptotic error estimate.

potential. Namely, for very small values of ε , the error is $O(\varepsilon)$. For intermediate values of ε , the error increases as the value of ε coincides with the spacing of the Gauss-Legendre quadrature points in the

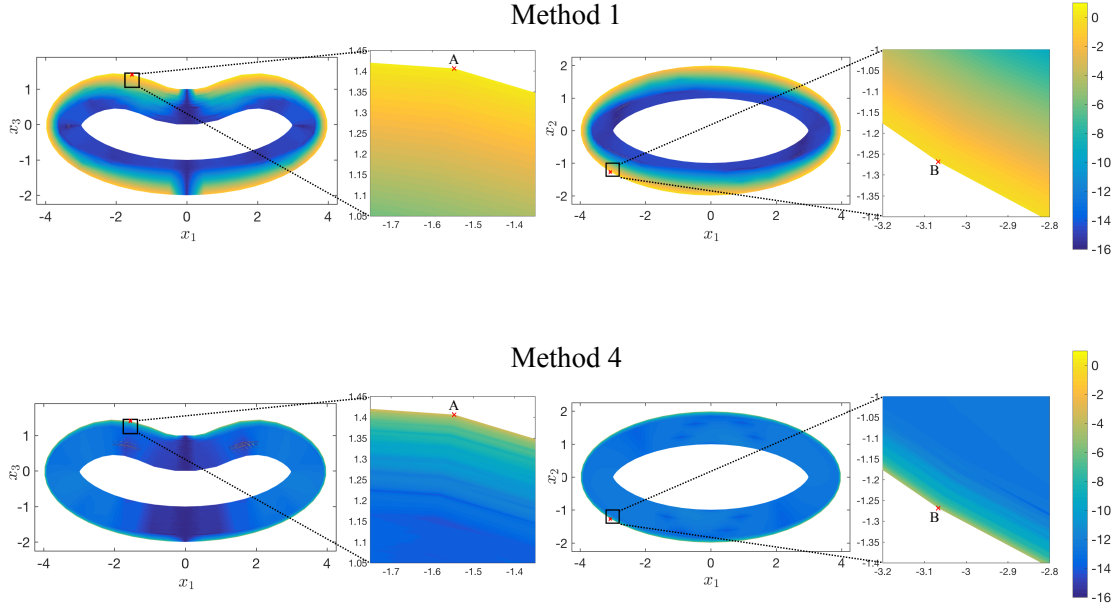


Figure 10: The errors made by Method 1 (top row) and Method 4 (bottom row) for the inverted mushroom cap, see Fig. 8, right. The first and second columns show \log_{10} of the errors made by these two methods in the x_1x_3 -plane with the plots in the second column showing a close-up in the vicinity of point A = $(-3.07, -1.27, 0)$. The third and fourth columns show \log_{10} of the errors made by these two methods over the x_1x_2 -plane with the plots in the fourth column showing a close-up in the vicinity of point B = $(-1.55, 0, 1.41)$.

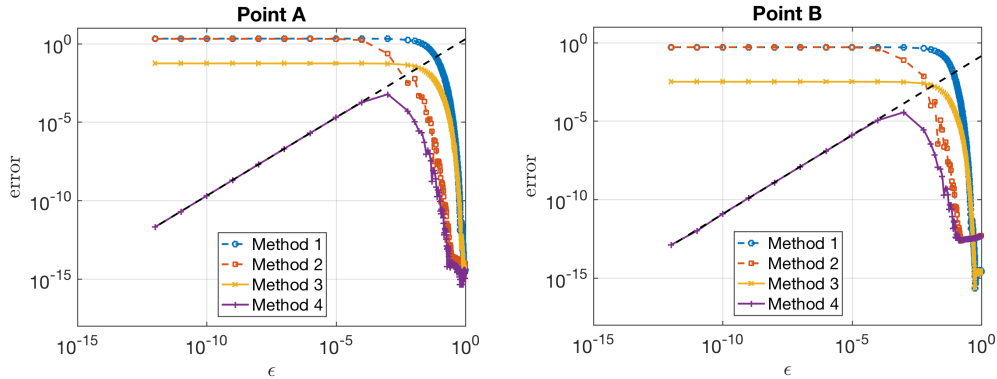


Figure 11: Comparison of errors made by Methods 1 – 4 for the inverted mushroom cap for evaluation points along the normal at distance ϵ from point A = $(-3.07, -1.27, 0)$ on the boundary and in the x_1x_3 -plane (left plot) and for evaluation points along the normal at distance ϵ from point B = $(-1.55, 0, 1.41)$ on the boundary and in the x_1x_2 -plane (right plot). The dashed, black lines show the best linear fit through the Method 4 errors for the four smallest ϵ values. For both fits, the slopes are consistent with the $O(\epsilon)$ asymptotic error estimate given by (3.18).

polar angle, s . For bigger values of ϵ , Methods 1, 2, 3, and 4 are all very accurate.

7 Conclusions

We have presented a simple and effective numerical method for the close evaluation of double- and single-layer potentials in three dimensions. The close evaluation of these layer potentials are challenging to numerically compute because they are nearly singular integrals. Based on a local analysis of these layer potentials about the point at which their kernel is sharply peaked, we have identified a natural way to compute those nearly singular integrals. This method consists of three steps:

1. Rotate the coordinate system so that the point at which the integrand is sharply peaked is aligned with the north pole.
2. Integrate first with respect to the azimuthal angle using the Periodic Trapezoid Rule.
3. Integrate the remaining function with respect to the polar angle using the Gauss-Legendre Quadrature Rule mapped from $[-1, 1]$ to $[0, \pi]$.

A key point to Step 3 is that we do not integrate with respect to the cosine of the polar angle because the factor of sine of the polar angle (the natural Jacobian for the spherical coordinate system) is important in effectively computing these integrals. Numerical results presented here show that the last step is essential for accurately computing these integrals. Moreover, the numerical results confirm the asymptotic analysis results: the error for the modified double-layer potential due to the subtraction method decreases quadratically with respect to the distance from the boundary and the error for the single-layer potential decreases linearly with respect to the distance from the boundary.

This method is effective because integration with respect to azimuth in the rotated coordinate system is a natural averaging operation leading to a smooth function in the polar angle. This averaging operation is a feature of the three-dimensional problem. It is not available for two-dimensional problems. The results from the local analysis given by (3.11) and (3.18) show that this azimuthal averaging yields a function in the polar angle that has a finite limit at the north pole of the rotated coordinate system. Rather than use these results in a quadrature rule for the polar angle, we have chosen to use the Gauss-Legendre Quadrature Rule, which is an open rule, so that the quadrature points never include the north and south poles. Therefore, these limiting values are not explicitly needed.

The local analysis used here can be extended to compute the full asymptotic expansions for the close evaluation of double- and single-layer potentials. These asymptotic expansions can be used to find approximations to a desired order of accuracy. Details of these asymptotic expansions can be found in [13]. These asymptotic expansions may be useful if one requires more accuracy for the close evaluation of layer potentials. Nonetheless, we find that $O(\varepsilon^2)$ asymptotic error estimate for the modified double-layer potential and the $O(\varepsilon)$ asymptotic error estimate for the single-layer potential to be quite accurate. An asymptotic expansion for the single-layer potential may be useful to obtain an asymptotic error that matches that of the modified double-layer potential, for example.

We have assumed that the boundary is closed, oriented, and analytic in this paper, but as long as the surface near the point on the boundary at which the integrand is singular is relatively smooth so that there exists a natural averaging operation, one can apply this approach. Doing so may require consideration of different quadrature rules for that specific context.

Finally, the analysis shown here can be extended to other problems. In particular, this method is broadly applicable to weakly singular and nearly singular integrals over two-dimensional surfaces. These weakly singular and nearly singular integrals may correspond to solutions of other elliptic partial differential equations including Helmholtz's equation and Stokes' equations.

A Rotations on the sphere

We give the explicit rotation formulas over the sphere used throughout this paper. Consider $y, y^* \in S^2$, the unit sphere. We introduce the parameters $\theta \in [0, \pi]$ and $\varphi \in [-\pi, \pi]$ and write

$$y = y(\theta, \varphi) = \sin \theta \cos \varphi \hat{i} + \sin \theta \sin \varphi \hat{j} + \cos \theta \hat{k}. \quad (\text{A.1})$$

The specific parameters θ^* and φ^* are set so that $y^* = y(\theta^*, \varphi^*)$. We would like to work in the rotated, uvw -coordinate system in which

$$\begin{aligned}\hat{u} &= \cos \theta^* \cos \varphi^* \hat{i} + \cos \theta^* \sin \varphi^* \hat{j} - \sin \theta^* \hat{k}, \\ \hat{v} &= -\sin \varphi^* \hat{i} + \cos \varphi^* \hat{j}, \\ \hat{w} &= \sin \theta^* \cos \varphi^* \hat{i} + \sin \theta^* \sin \varphi^* \hat{j} + \cos \theta^* \hat{k}.\end{aligned}\tag{A.2}$$

In this rotated system we have $\hat{w} = y^*$. For this rotated coordinate system, we introduce the parameters $s \in [0, \pi]$ and $t \in [-\pi, \pi]$ such that

$$y = y(s, t) = \sin s \cos t \hat{u} + \sin s \sin t \hat{v} + \cos s \hat{w}.\tag{A.3}$$

It follows that $\hat{w} = y^* = y(0, \cdot)$. This corresponds to setting y^* to be the north pole. By equating (A.1) and (A.3) and substituting (A.2) into that result, we obtain

$$\begin{bmatrix} \sin \theta \cos \varphi \\ \sin \theta \sin \varphi \\ \cos \theta \end{bmatrix} = \begin{bmatrix} \cos \theta^* \cos \varphi^* & -\sin \varphi^* & \sin \theta^* \cos \varphi^* \\ \cos \theta^* \sin \varphi^* & \cos \varphi^* & \sin \theta^* \sin \varphi^* \\ -\sin \theta^* & 0 & \cos \theta^* \end{bmatrix} \begin{bmatrix} \sin s \cos t \\ \sin s \sin t \\ \cos s \end{bmatrix}.\tag{A.4}$$

Let us rewrite (A.4) compactly as $y(\theta, \varphi) = R(\theta^*, \varphi^*)y(s, t)$ with $R(\theta^*, \varphi^*)$ denoting the 3×3 matrix given above. It is a rotation matrix. Hence, it is orthogonal.

We now seek to write $\theta = \theta(s, t)$ and $\varphi = \varphi(s, t)$. To do so, we introduce

$$\xi(s, t; \theta^*, \varphi^*) = \cos \theta^* \cos \varphi^* \sin s \cos t - \sin \varphi^* \sin s \sin t + \sin \theta^* \cos \varphi^* \cos s,\tag{A.5}$$

$$\eta(s, t; \theta^*, \varphi^*) = \cos \theta^* \sin \varphi^* \sin s \cos t + \cos \varphi^* \sin s \sin t + \sin \theta^* \sin \varphi^* \cos s,\tag{A.6}$$

$$\zeta(s, t; \theta^*, \varphi^*) = -\sin \theta^* \sin s \cos t + \cos \theta^* \cos s.\tag{A.7}$$

From (A.5) - (A.7), we find that

$$\theta = \arctan \left(\frac{\sqrt{\xi^2 + \eta^2}}{\zeta} \right),\tag{A.8}$$

and

$$\varphi = \arctan \left(\frac{\eta}{\xi} \right).\tag{A.9}$$

B Spherical Laplacian

In this Appendix, we establish the result given in (3.10). We first seek an expression for $\partial_s^2[\cdot]|_{s=0}$ in terms of θ and φ . By the chain rule, we find that

$$\frac{\partial^2}{\partial s^2}[\cdot] \Big|_{s=0} = \left[\left(\frac{\partial \theta}{\partial s} \right)^2 \frac{\partial^2}{\partial \theta^2} + \left(\frac{\partial \varphi}{\partial s} \right)^2 \frac{\partial^2}{\partial \varphi^2} + 2 \frac{\partial \theta}{\partial s} \frac{\partial \varphi}{\partial s} \frac{\partial^2}{\partial \theta \partial \varphi} + \frac{\partial^2 \theta}{\partial s^2} \frac{\partial}{\partial \theta} + \frac{\partial^2 \varphi}{\partial s^2} \frac{\partial}{\partial \varphi} \right] \Big|_{s=0}.\tag{B.1}$$

Using θ defined in (A.8) and φ defined in (A.9), we find that

$$\frac{\partial \theta(s, t)}{\partial s} \Big|_{s=0} = \cos t,\tag{B.2}$$

$$\frac{\partial^2 \theta(s, t)}{\partial s^2} \Big|_{s=0} = \frac{\cos \theta^*}{\sin \theta^*} \sin^2 t,\tag{B.3}$$

$$\frac{\partial \varphi(s, t)}{\partial s} \Big|_{s=0} = \frac{\sin t}{\sin \theta^*},\tag{B.4}$$

$$\frac{\partial^2 \varphi(s, t)}{\partial s^2} \Big|_{s=0} = -\frac{\cos \theta^*}{\sin^2 \theta^*} \sin 2t.\tag{B.5}$$

Note that at $s = 0$, we have $\theta^* = \theta$.

Substituting (B.2) – (B.5) into (B.1) and replacing θ^* by θ , we obtain

$$\left. \frac{\partial^2}{\partial s^2} [\cdot] \right|_{s=0} = \cos^2 t \frac{\partial^2}{\partial \theta^2} + \sin^2 t \frac{1}{\sin^2 \theta} \frac{\partial^2}{\partial \varphi^2} + 2 \cos t \sin t \frac{1}{\sin \theta} \frac{\partial^2}{\partial \theta \partial \varphi} + \sin^2 t \frac{\cos \theta}{\sin \theta} \frac{\partial}{\partial \theta} - \sin 2t \frac{\cos \theta}{\sin^2 \theta} \frac{\partial}{\partial \varphi}, \quad (\text{B.6})$$

from which it follows that

$$\frac{1}{\pi} \int_0^\pi \left. \frac{\partial^2}{\partial s^2} [\cdot] \right|_{s=0} dt = \frac{1}{2} \left[\frac{\partial^2}{\partial \theta^2} + \frac{\cos \theta}{\sin \theta} \frac{\partial}{\partial \theta} + \frac{1}{\sin^2 \theta} \frac{\partial^2}{\partial \varphi^2} \right] = \frac{1}{2} \Delta_{S^2}, \quad (\text{B.7})$$

which establishes the result.

Acknowledgments

This research was supported by National Science Foundation Grant: DMS-1819052. A. D. Kim is also supported by the Air Force Office of Scientific Research Grant: FA9550-17-1-0238.

References

- [1] L. af Klinteberg, A.-K. Tornberg, A fast integral equation method for solid particles in viscous flow using quadrature by expansion, *J. Comput. Phys.* 326 (2016) 420–445.
- [2] L. af Klinteberg, A.-K. Tornberg, Error estimation for quadrature by expansion in layer potential evaluation, *Adv. Comput. Math.* 43 (1) (2017) 195–234.
- [3] K. E. Atkinson, Numerical integration on the sphere, *ANZIAM J.* 23 (3) (1982) 332–347.
- [4] K. E. Atkinson, The numerical solution Laplace’s equation in three dimensions, *SIAM J. Numer. Anal.* 19 (2) (1982) 263–274.
- [5] K. E. Atkinson, Algorithm 629: An integral equation program for Laplace’s equation in three dimensions, *ACM Trans. Math. Softw.* 11 (2) (1985) 85–96.
- [6] K. E. Atkinson, A survey of boundary integral equation methods for the numerical solution of Laplace’s equation in three dimensions, in: *Numerical Solution of Integral Equations*, Springer, 1990, pp. 1–34.
- [7] K. E. Atkinson, *The Numerical Solution of Integral Equations of the Second Kind*, Cambridge University Press, 1997.
- [8] A. H. Barnett, Evaluation of layer potentials close to the boundary for Laplace and Helmholtz problems on analytic planar domains, *SIAM J. Sci. Comput.* 36 (2) (2014) A427–A451.
- [9] J. T. Beale, M.-C. Lai, A method for computing nearly singular integrals, *SIAM J. Numer. Anal.* 38 (6) (2001) 1902–1925.
- [10] J. T. Beale, W. Ying, J. R. Wilson, A simple method for computing singular or nearly singular integrals on closed surfaces, *Commun. Comput. Phys.* 20 (3) (2016) 733–753.
- [11] O. P. Bruno, L. A. Kunyansky, A fast, high-order algorithm for the solution of surface scattering problems: basic implementation, tests, and applications, *J. Comput. Phys.* 169 (1) (2001) 80–110.
- [12] C. Carvalho, S. Khatri, A. D. Kim, Asymptotic analysis for close evaluation of layer potentials, *J. Comput. Phys.* 355 (2018) 327–341.

- [13] C. Carvalho, S. Khatri, A. D. Kim, Asymptotic approximation for the close evaluation of double-layer potentials, In preparation.
- [14] L. M. Delves, J. L. Mohamed, Computational Methods for Integral Equations, Cambridge University Press, 1988.
- [15] C. L. Epstein, L. Greengard, A. Klöckner, On the convergence of local expansions of layer potentials, *SIAM J. Numer. Anal.* 51 (5) (2013) 2660–2679.
- [16] R. B. Guenther, J. W. Lee, Partial Differential Equations of Mathematical Physics and Integral Equations, Dover Publications, 1996.
- [17] J. Helsing, R. Ojala, On the evaluation of layer potentials close to their sources, *J. Comput. Phys.* 227 (5) (2008) 2899–2921.
- [18] A. Klöckner, A. Barnett, L. Greengard, M. O’Neil, Quadrature by expansion: A new method for the evaluation of layer potentials, *J. Comput. Phys.* 252 (2013) 332–349.
- [19] M. Rachh, A. Klöckner, M. O’Neil, Fast algorithms for quadrature by expansion i: Globally valid expansions, *J. Comput. Phys.* 345 (2017) 706–731.
- [20] C. Schwab, W. Wendland, On the extraction technique in boundary integral equations, *Math. Comput.* 68 (225) (1999) 91–122.
- [21] M. Wala, A. Klöckner, A fast algorithm for Quadrature by Expansion in three dimensions, [arXiv:1805.06106v1](https://arxiv.org/abs/1805.06106v1).